





Simulation of Impedance Changes with Aging in Lithium Titanate-based Cells Using Physics-Based Dimensionless Modeling

Anudeep Mallarapu,^{1,z}  Shriram Santhanagopalan,¹ Wataru Uno,² Yuta Kanai,² Yohei Uemura,³  Ryosuke Yagi,² and Shuichi Uchikoga³

¹Center for Energy Conversion & Storage Systems, National Renewable Energy Laboratory, Golden, Colorado, United States of America

²Corporate Research & Development Center, Toshiba Corporation, Japan

³Battery Division, Toshiba Corporation, Japan

Quantifying aging effects in lithium-ion cells with chemistries that have a flat open circuit potential is challenging. We implement a physics-based electrochemical model to track changes in the electrochemical impedance response of lithium titanate-based cells. Frequency domain equations of a pseudo two-dimensional model are made dimensionless, and the corresponding non-dimensional parameters are estimated using a Levenberg-Marquardt routine. The model weighs the relative contributions of changes in diffusion, ionic conduction within the electrolyte phase against solid phase electronic conduction towards cell aging. Solid-phase diffusion, charge transfer resistance and double layer capacitance at the solid-liquid interface are accounted for in the particle impedance. The estimation routine tracks dimensionless parameters using accelerated cycling data from full cells over 1000 cycles. The model can be deployed within a short time for state estimation using physics-based models without requiring prior knowledge of the battery chemistry, format, or capacity.

© 2023 The Author(s). Published on behalf of The Electrochemical Society by IOP Publishing Limited. This is an open access article distributed under the terms of the Creative Commons Attribution 4.0 License (CC BY, <http://creativecommons.org/licenses/by/4.0/>), which permits unrestricted reuse of the work in any medium, provided the original work is properly cited. [DOI: 10.1149/1945-7111/acf52a]



Manuscript submitted May 22, 2023; revised manuscript received August 14, 2023. Published September 13, 2023. *This paper is part of the JES Focus Issue on Multiscale Modeling, Simulation and Design: In Honor of Ralph E. White.*

Supplementary material for this article is available [online](#)

Reliable and high-capacity energy storage is essential for transitioning to renewable energy sources. Improving performance under fast charging and ability predict battery aging are extremely important to enable electrification in automotive, aerospace, and stationary applications. Electrochemical Impedance Spectroscopy (EIS) is a very common method to understand and characterize Li-ion batteries.¹ The impedance spectrum generated by this method depends on internal processes such as charge transfer kinetics, transport through solid electrolyte interface (SEI), electrolyte transport and solid phase diffusion. The response varies with temperature, state of charge (SOC) and state of health (SOH). Hence EIS is a simple yet powerful technique that can provide valuable information about a battery cell like SOC and SOH.²

One of the major limiting factors for wide scale adoption electric vehicles is the time it takes to charge batteries. Fast charging of batteries is limited by factors such as electrolyte transport, interfacial resistance and solid phase diffusion and can often lead to battery degradation.^{3,4} Degradation in lithium-ion batteries can attributed to several physical and chemical processes like SEI growth, lithium plating,⁴ positive electrode degradation and particle cracking, which lead to observable effects such as capacity fade and power fade.⁵ Advanced diagnostic techniques and detailed models have been used to study and understand each of these mechanisms leading to battery failure.^{6–8} But such studies often involve detailed analysis of cell components obtained from teardowns. While there is tremendous interest in tracking degradation with a just a simple non-destructive test like EIS, it is often quite challenging to tease out the effects of these processes from just full-cell experimental data.

Previous studies have used circuit models to estimate degradation of batteries using EIS data.^{9–12} They provide limited insights into physical parameters within the battery and are also difficult to extend to newer battery chemistries. Using physics-based models on the other hand, provides better understanding of each physical processes within the battery. Pseudo two-dimensional models have long been

used to model and study various aspects of lithium-ion batteries.^{13,14} Extensive research has been performed on modified forms of these “Newman” models, applying them to various application¹⁵ along with improvements to its computational efficiency.^{16,17} These models have been mostly used in time-domain form for understanding battery performance, reliability, and safety.^{18–20} However, use of these models requires tracking a large number of parameters related to phenomena such as electrochemical reaction rates, species conservation and charge conservation, in solid and electrolyte phase.

Several approaches have been used to obtain impedance response from electrochemical models. Even though it is more common to use equivalent circuit models to estimate impedance response of batteries, it does not provide sufficient understanding of physical parameters that change within the battery. Weddle et al. have used a stitching algorithm to estimate battery impedance spectra using stitching algorithm using on a composite state space model.²¹ Based on initial frequency domain modeling efforts,^{22,23} researchers have used porous electrode theory to simulate impedance response of lithium-ion cells.^{24,25} Pathak et al. have used direct estimation of impedance spectra by solving frequency domain equations of a porous electrode model.²⁶ The approach we present here is similar, but with modified equations containing non-dimensional groups.

Use of non-dimensional groups has been previously used to analyze performance of batteries.^{27,28} The use of dimensionless groups has several advantages: when all parameters for an electrochemical model are available, one can use a traditional “Newman-type” model, but often there are restrictions on what parameters we have access to. The use of dimensionless groups helps us pursue a physics-based model with a limited number of parameters known a priori. The use of dimensionless groups also helps us to assess the relative contributions of the different physical phenomena (e.g., diffusion flux vs migration flux or solid-phase transport Vs electrolyte transport, etc.) towards the degradation of the cells. We start with a Newman type pseudo two-dimensional electrochemical model and present the approach to develop non-dimensional groups for dimensionless analysis. This model is then used to study degradation in full cells with an LTO anode, at various number of

^zE-mail: Anudeep.Mallarapu@nrel.gov

Table II. Definitions of dimensionless groups (used in Table I) and related expressions.

$k = p, n$	$\Theta_{1,k} = \frac{j^* l_k^2 a_k F}{\phi^* \sigma_k^{\text{eff}}}$	$\Theta_1 = \frac{j^* l_c^2 a_n F}{\phi^* \sigma_n^{\text{eff}}}$	$\Theta_{7,k} = \frac{\phi^*}{R_{ct,k} F j^*}$	$\Theta_{7,n} = \frac{\phi^*}{R_{ct,n} F j^*}$	$\Theta_{11,k} = \frac{l_k}{l_s}$
		$\Theta_{1,n} = \Theta_1 \Theta_{11,n}^2$		$\Theta_{7,p} = \frac{\phi^*}{R_{ct,p} F j^*}$	
	$\Theta_{2,k} = \frac{l_k I_{app}}{\phi^* \sigma_k^{\text{eff}}}$	$\Theta_2 = \frac{l_s I_{app}}{\phi^* \sigma_n^{\text{eff}}}$	$\Theta_{8,k} = C_{dl,k} \frac{\omega^* \phi^*}{F j^*}$	$\Theta_{8,n} = C_{dl,n} \frac{\omega^* \phi^*}{F j^*}$	$\Theta_{12,k} = \frac{\epsilon_k}{\epsilon_s}$
		$\Theta_{2,n} = \Theta_2 \Theta_{11,n}$		$\Theta_{8,p} = C_{dl,p} \frac{\omega^* \phi^*}{F j^*}$	
	$\Theta_{3,k} = \frac{\sigma_k^{\text{eff}}}{\kappa_e \epsilon_k^b}$	$\Theta_3 = \frac{\sigma_n^{\text{eff}}}{\kappa_e \epsilon_s^b}$	$\Theta_{9,k} = \frac{R_{part,k}}{R_{ct,k}}$	$\Theta_{9,n} = \frac{R_{part,n}}{R_{ct,n}}$	$\Theta_{13} = \frac{\sigma_p^{\text{eff}}}{\sigma_n^{\text{eff}}}$
		$\Theta_{3,n} = \Theta_3 \Theta_{12,n}^{-b}$		$\Theta_{9,p} = \frac{R_{part,p}}{R_{ct,p}}$	
	$\Theta_4 = \frac{2RT(1-t_+)e^*}{F c_0 \phi^*}$	$\Theta_{3,p} = \Theta_3 \Theta_{12,p}^{-b} \Theta_{13}$	$\Theta_{10,k} = \frac{D_{s,k}}{\omega^* R_{s,k}^2}$	$\Theta_{10,n} = \frac{D_{s,n}}{\omega^* R_{s,n}^2}$	$\Theta_{14} = \frac{a_p}{a_n}$
				$\Theta_{10,p} = \frac{D_{s,p}}{\omega^* R_{s,p}^2}$	
	$\Theta_5 = \frac{a_k j^* (1-t_+)}{\epsilon_k \kappa^* \omega^*}$	$\Theta_5 = \frac{a_n j^* (1-t_+)}{\epsilon_s \kappa^* \omega^*}$			$\Theta_{15} = b$
		$\Theta_{5,n} = \Theta_5 \Theta_{12,n}^{-1}$			
		$\Theta_{5,p} = \Theta_5 \Theta_{14} \Theta_{12,p}^{-1}$			
$k = p, n, s$	$\Theta_{6,k} = \frac{D_e \epsilon_k^{b-1}}{\omega^* l_k^2}$	$\Theta_6 = \frac{D_e \epsilon_s^{b-1}}{\omega^* l_s^2}$			
		$\Theta_{6,s} = \Theta_6$			
		$\Theta_{6,n} = \Theta_6 \Theta_{12,n}^{b-1} \Theta_{11,n}^{-2}$			
		$\Theta_{6,p} = \Theta_6 \Theta_{12,p}^{b-1} \Theta_{11,p}^{-2}$			

$$\omega = \Omega \omega^* \quad [10]$$

$$x = X x^* \quad [11]$$

We take x^* as l_n, l_s, l_p in negative electrode, separator, and positive electrode respectively. The model equations in their non-dimensional form are provided in Table I with corresponding definitions of dimensionless parameters in Table II.

The dimensionless impedance can now be defined as follows:

$$\begin{aligned} (\bar{Z}_{cell}) &= \left(A_0 \frac{I_{app}}{\phi^*} \right) Z_{cell} \\ &= \left(\frac{A_0 \sigma_p^{\text{eff}}}{l_p} \Theta_{2,p} \right) Z_{cell} = [\Phi_1]_{X=3} - [\Phi_1]_{X=0} \end{aligned} \quad [12]$$

$$\bar{Z}_{cell} = Z^* \cdot Z_{cell} \quad [13]$$

This model has a total of 21 independent non-dimensional parameters. A dimensional parameter (Z^*) is also required to compare model results (dimensionless \bar{Z}_{cell}) to experimental data ($(Z_{cell})^{\text{dat}}$ in Ohms), bringing the total model parameters to 22.

$\Theta_1, \Theta_2, \Theta_3, \Theta_4, \Theta_5, \Theta_6, \Theta_{7,p}, \Theta_{8,p}, \Theta_{9,p}, \Theta_{10,p}, \Theta_{7,n}, \Theta_{8,n}, \Theta_{9,n}, \Theta_{10,n}, \Theta_{11,n}, \Theta_{11,p}, \Theta_{12,n}, \Theta_{12,p}, \Theta_{13}, \Theta_{14}, \Theta_{15}, Z^*$ where Θ_i are defined in Table II. It should be noted that for Θ_1 to Θ_6 the values in different regions can be related using other dimensionless variables as shown in Table III. Θ_7 to Θ_{10} are independent parameters in positive and negative electrode regions. The equations in Table I are discretized using the finite difference method and the dimensionless variables are solved for each point across a range of frequencies. Simpler closed-form solutions are possible. See for example.²⁹

Experimental data and parameter estimation process.—For this study, a 1 Ah-class pouch cell (LTO/NMC811) is assembled for accelerated degradation test. The NMC811 positive electrode with LiNi0.8Mn0.1Co0.1O₂, carbon, and polyvinylidene fluoride is prepared with a density of 3 g cc⁻¹. The LTO negative electrode with LTO, carbon, and polyvinylidene fluoride is prepared and with a density of 2 g cc⁻¹. These electrodes are then dried in vacuum at a temperature of 120 °C. The pouch cell is assembled using same protocol in Ref. 30. An electrochemical cycling test is conducted between 2.75 V and 1.5 V using a constant-current/constant-voltage charge (CCCV-charge) protocol, followed by a constant-current discharge (CC-discharge) protocol in a thermostat chamber set to 65 °C. The charging and discharging load current of 3C-rate is used and the termination current during CV charge is set to C/20. The AC impedance of the cell is measured at 25 °C on a combined potentiostat and frequency response analyzer (Solartron 1287 A by Solartron Analytical) every 200th cycle with a voltage amplitude of 10 mV vs 2.25 V (open circuit voltage at SOC50% of the cell), with frequencies ranging from 4.8 kHz to 0.05 Hz used in the analysis. For subsequent analysis, the inductance component is removed from the raw data. For this, raw data is fitted to an equivalent circuit model (see supplementary document for more information). The inductance component is then subtracted from the raw data using the following equation.

$$Z_{dat} = Z_{raw} - \frac{2\pi\nu_i L R_L}{R_L + 2\pi\nu_i L} \quad [14]$$

where Z_{raw} and Z_{dat} are raw impedance data and inductance corrected impedance data respectively, ν_i is frequency, L and R_L are inductance parameters in equivalent circuit model.

The model parameters are estimated using Levenberg–Marquardt algorithm³¹ by minimizing sum of the weighted squares of the errors (χ^2) where error is the difference between model prediction (for a parameter set \vec{p}) and experimental data for each frequency (ν_i). In

Table III. Variables used in this paper.

Variable	Description	SI units
ϕ_1	Solid phase potential	V
ϕ_2	Liquid phase potential	V
c_1	Solid phase lithium concentration	mol/m ³
c_2	Liquid phase lithium concentration	mol/m ³
j	Lithium flux at interface	mol/s/m ²
<i>Positive</i>	<i>Negative</i>	
$R_{s,p}$	$R_{s,n}$	Particle radius m
$D_{s,p}$	$D_{s,n}$	Solid phase diffusivity m ² /s
$i_{0,p}$	$i_{0,n}$	Exchange current density A/m ²
$\alpha_{A,p}$	$\alpha_{A,n}$	Anodic charge transfer coefficient —
$\alpha_{C,p}$	$\alpha_{C,n}$	Cathodic charge transfer coefficient —
$C_{dl,p}$	$C_{dl,n}$	Double layer capacitance F/m ²
$\left(\frac{dU}{dc_s}\right)_p$	$\left(\frac{dU}{dc_s}\right)_n$	Derivative of open circuit potential V m ³ /mol
a_p	a_n	Area fraction m ² /m ³
σ_p^{eff}	σ_n^{eff}	Effective electronic conductivity S/m
l_p	l_n	Electrode thickness m
ϵ_p	ϵ_n	Electrode porosity m ³ /m ³
c_0		Electrolyte salt concentration mol/m ³
D_e		Electrolyte diffusivity m ² /s
κ_e		Electrolyte ionic conductivity S/m
l_s		Separator thickness m
ϵ_s		Separator porosity m ³ /m ³
b		Bruggeman coefficient —
t_{Li^+}		Lithium-ion transference number —
R		Gas constant J/mol/K
F		Faraday constant s A/mol
T		Temperature K
I_{app}		Applied current amplitude A
A_0		Cell area m ²

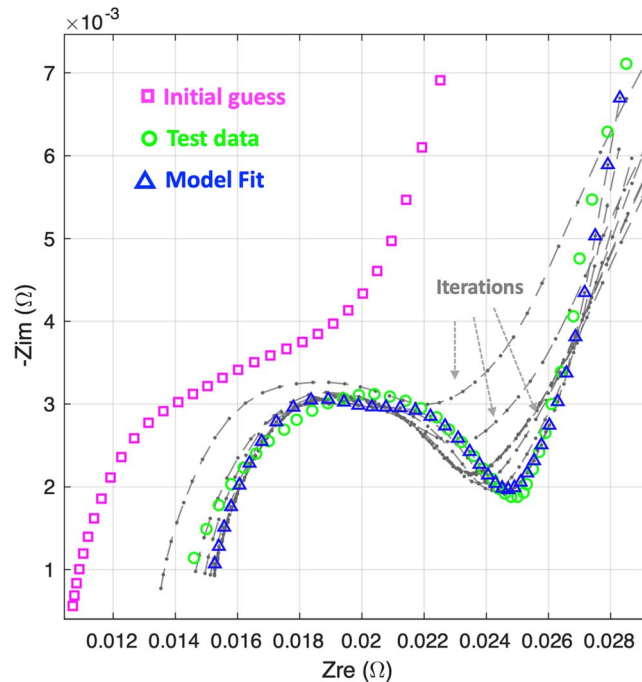


Figure 1. Fitting using Levenberg–Marquardt parameter estimation algorithm: The impedance model is fit to experimental EIS data by starting from a reasonable initial guess.

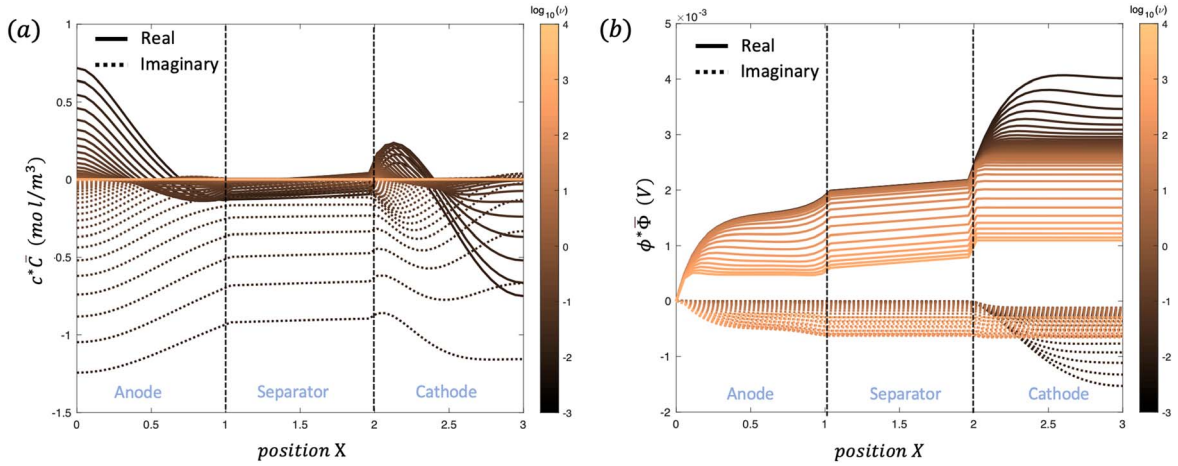


Figure 2. Sample profiles of oscillation in (a) electrolyte concentration and (b) electrolyte potential predicted using the model used in this work. These profiles are real and imaginary components of oscillation around equilibrium values.

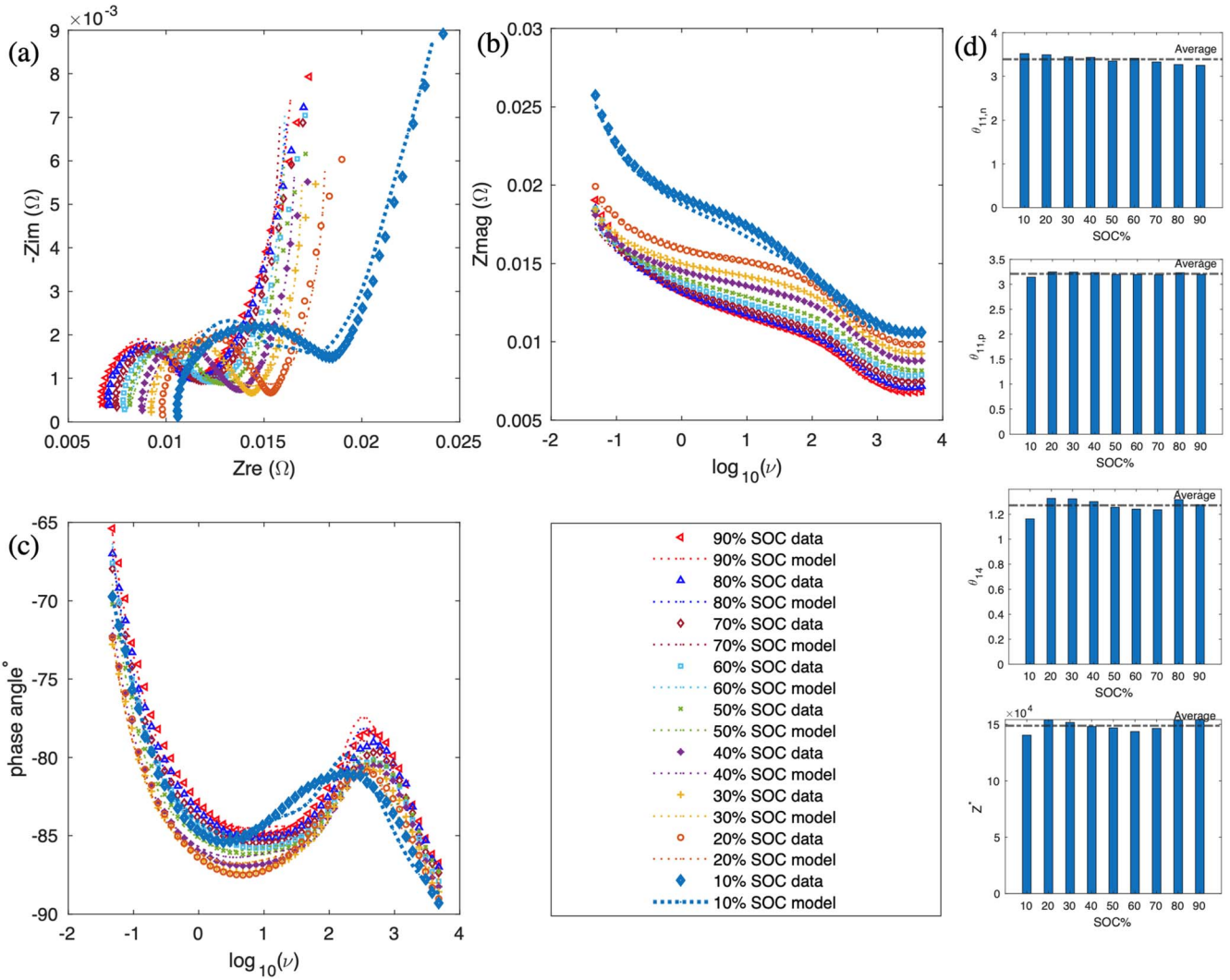


Figure 3. Model fits compared against experimental results for dataset A. (a) Nyquist plot (b) magnitude of complex cell impedance (c) phase angle of impedance (d) Z^* , $\theta_{11,p}$, $\theta_{11,n}$, θ_{14} values predicted for each state of charge in this data set.

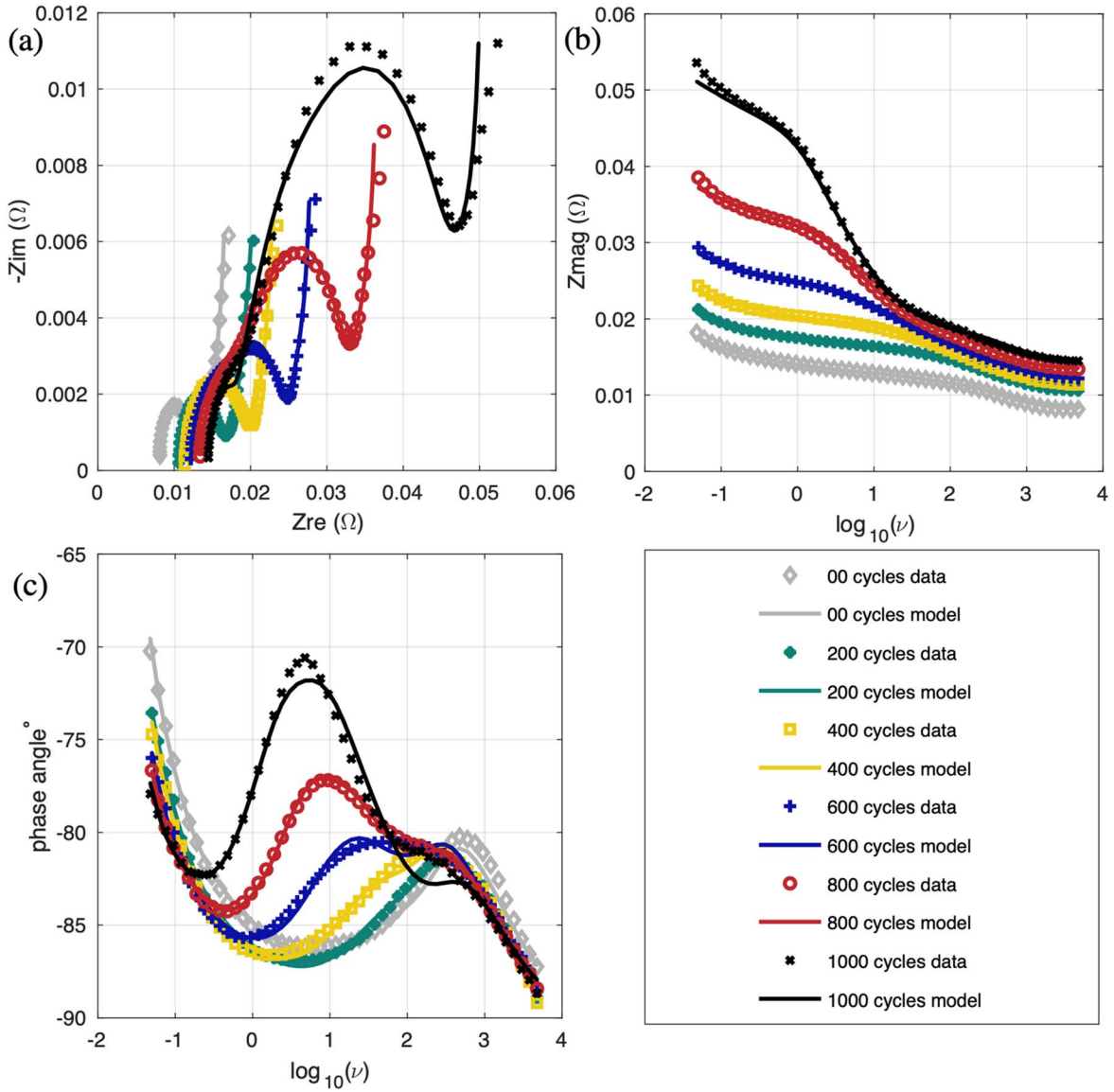


Figure 4. Model fit compared against experimental data for dataset B (a) Nyquist plot (b) magnitude of complex cell impedance (c) phase angle of impedance.

this case \vec{p} is the set of 22 parameters as described in the previous section (Mathematical model development).

$$\chi^2(\vec{p}) = \frac{\sum_{\nu_i} (|Z^m(\vec{p})| - |Z^{dat}|)^2}{\sum_{\nu_i} |Z^{dat}|^2} + \frac{\sum_{\nu_i} (\varphi_Z^m(\vec{p}) - \varphi_Z^{dat})^2}{\sum_{\nu_i} (\varphi_Z^{dat})^2} \quad [15]$$

where the phase angle (φ_Z) is defined as

$$\varphi_Z = \tan^{-1}\left(\frac{\text{Im}(Z)}{\text{Re}(Z)}\right) \quad [16]$$

There can be several non-unique sets of parameters which will produce the same output EIS data. For example, increasing Θ_p by δ_1 can have the same effect on the impedance curve as decreasing Θ_q by δ_2 . Which means a single EIS experiment does not provide all the necessary information to estimate all the model parameters. Hence it is necessary to fit the data across multiple data sets to get a more accurate value for each parameter. For accurate parameter estimation

it is important to understand which parameters change across the available experimental data.

It is reasonable to assume that Z^* , which is determined by total cell area, does not change much for the cells of the same type and size. Similarly, $\Theta_{11,k}$ and Θ_{14} also remain constant for a battery unless extremely large expansions/deformations occur. The parameter estimation algorithm will optimize these to minimize the error to a minimum for each test. Hence, we first use the parameter estimation algorithm over dataset A (EIS data on uncycled cells at multiple SOCs) by including these parameters (Z^* , $\Theta_{11,p}$, $\Theta_{11,n}$, Θ_{14}) as a variable parameter. Average predicted values from parameter estimation on dataset A for these parameters are held fixed when analyzing dataset B (EIS data on the same type of cells cycled to multiple number of cycles). Approximate initial guesses are used from parameters provided in Ref. 26. Figure 1 shows a sample case for how initial model prediction gets fitted the measured data as algorithmic iterations progress.

It is important that parameter estimation algorithm finds physically meaningful values while ensuring goodness of fit against the data. For instance, physical parameters like electrode thicknesses and porosities cannot change by orders of magnitude when the

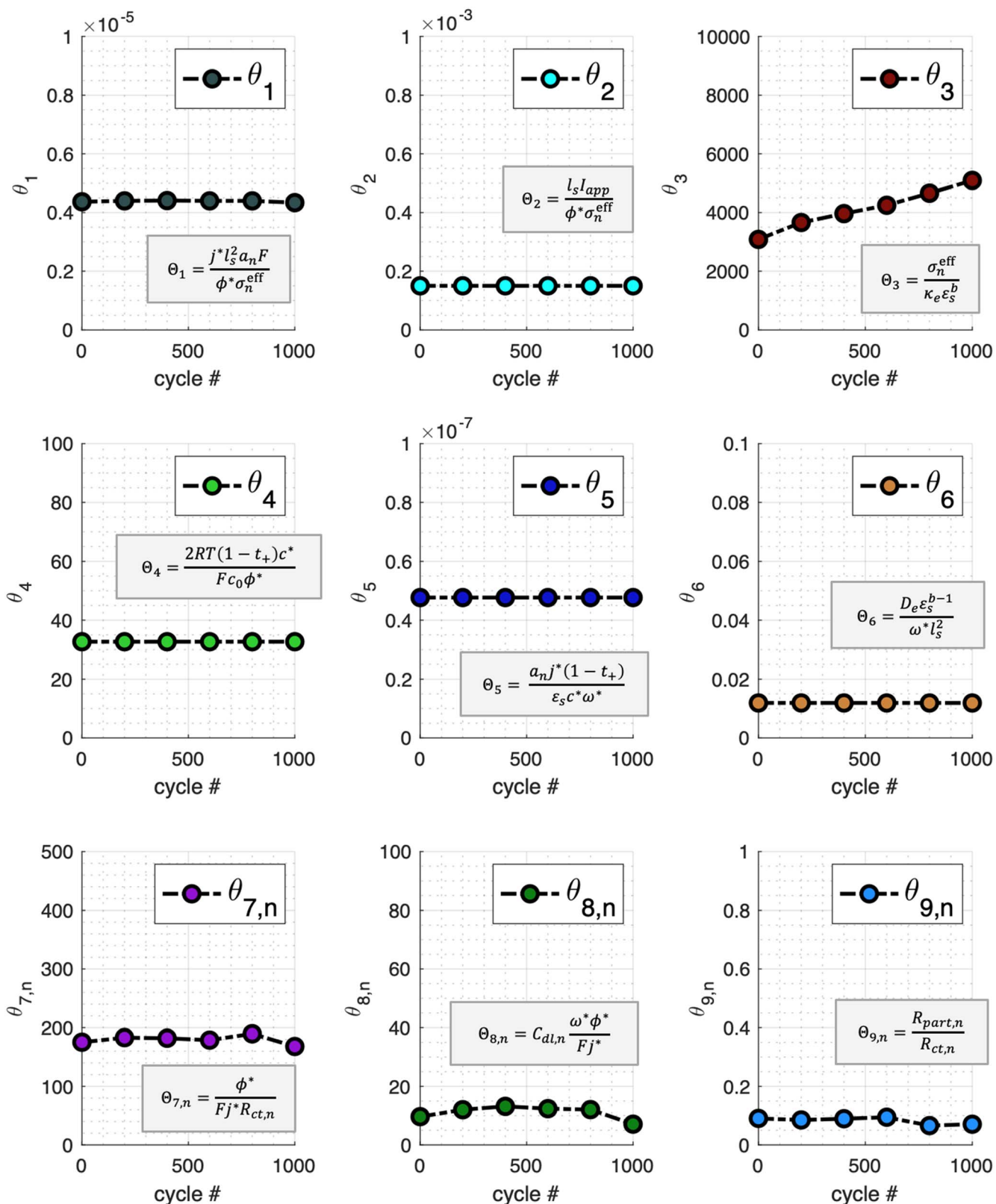


Figure 5. Trends in dimensionless parameters – I.

capacity degradation from the cell is gradual. To make sure that the model parameters are realistic, an initial run of optimization was performed, fixing the parameters θ_1 , θ_4 , θ_5 , θ_6 , θ_{12} . The final set of estimates were performed by including all parameters within the estimation routine.

Results and Discussion

The solution for the spatial distribution of variables as a function of applied frequency as shown in Fig. 2. Negative values in these plots are a result of the oscillations in the variables not being in-phase with the applied current oscillation. The variation in of both \bar{C}_2

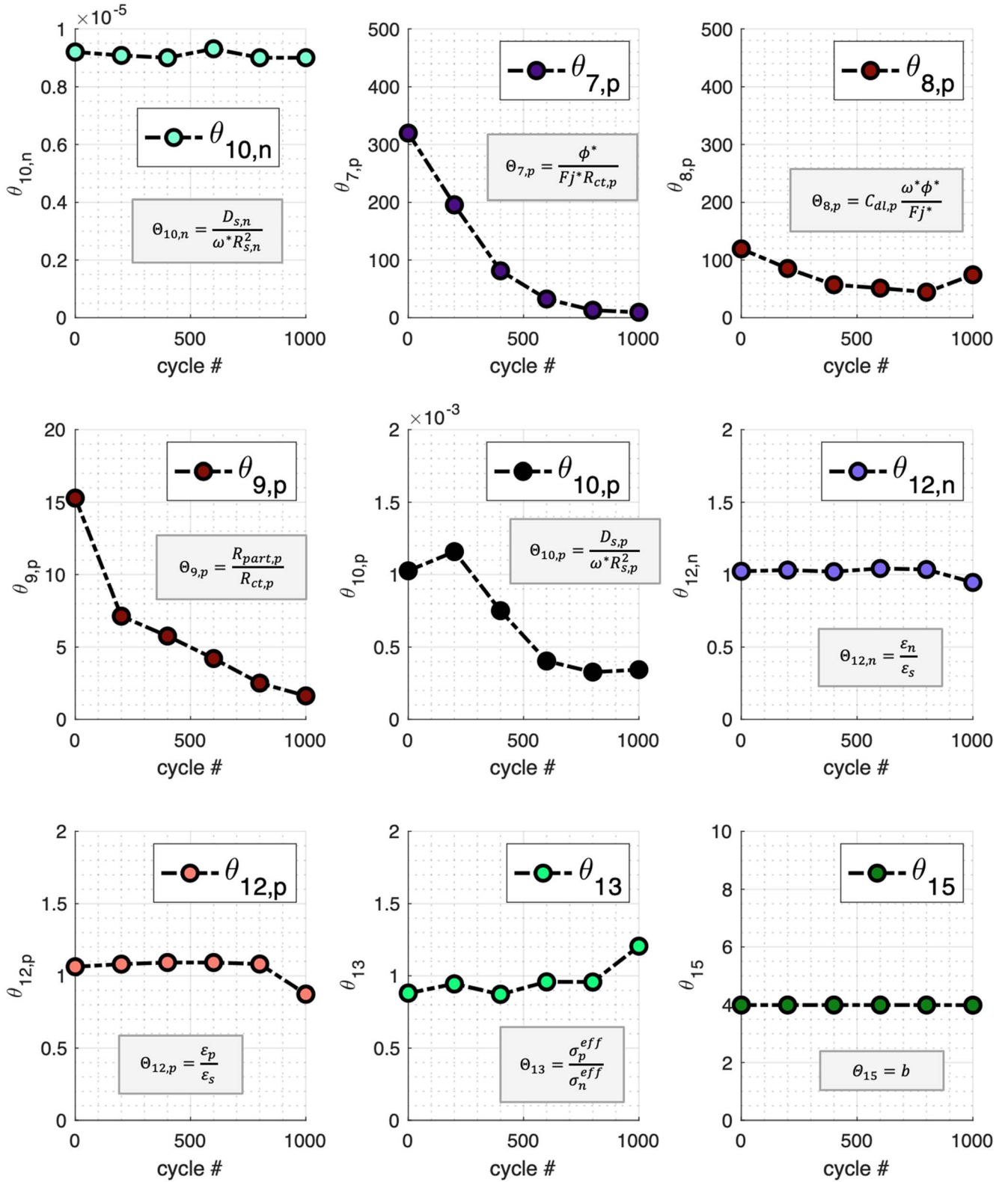


Figure 6. Trends in dimensionless parameters – II.

and Φ_2 is linear in the separator region. At very high frequencies, the oscillations in lithium concentration (Fig. 2a) drop to almost zero, since there is not enough time available for mass transfer to take place. The magnitude of oscillation in electrolyte potential (Fig. 2b) steadily decreases as frequency of applied current increases. It should be noted that Fig. 2a is depicting real and imaginary parts of

small oscillations around equilibrium concentration which do not contribute to overall depletion/accumulation of salt concentration.

This model runs quickly (Using 2.4 GHz Intel Core i9 processor with 16 GB memory, the simulation of an EIS curve with 41 data points typically takes around 2.408 s which is roughly 60 ms for each frequency point) and can obtain the impedance response across a wide

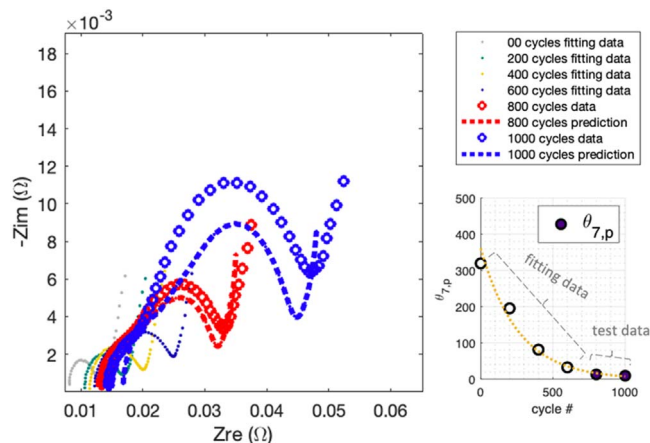


Figure 7. Approach to predict EIS spectrum from parameter trends: fits from initial cycles are extrapolated to predict parameters for subsequent number of cycles.

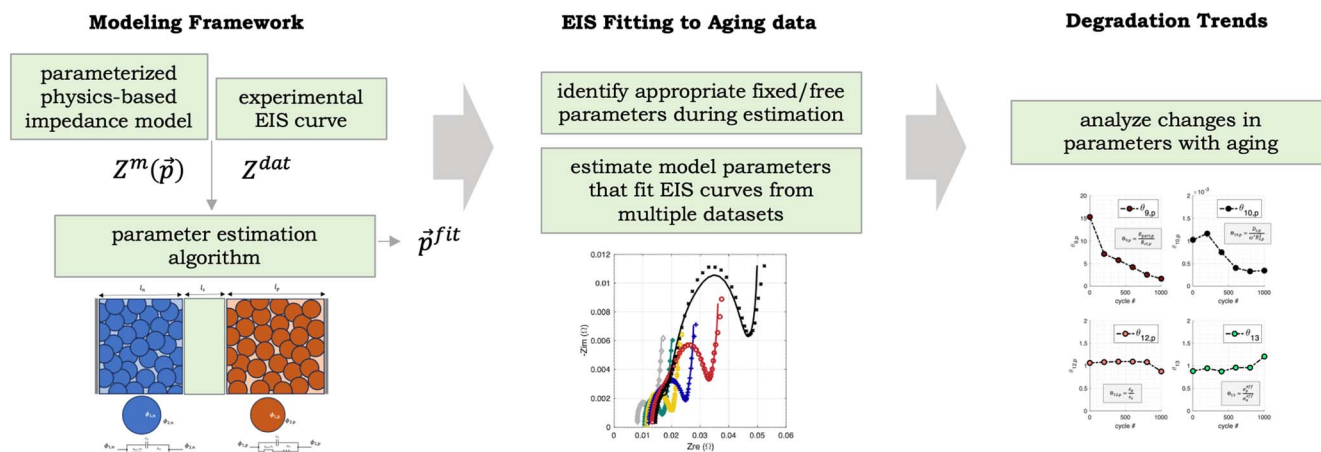


Figure 8. Summary of the approach used in current study. The developed framework is useful to quickly understand physical changes under aging conditions, using EIS data.

range of frequencies. As we increase frequency, the imaginary part of impedance approaches zero and electronic effects dominate, which is expected. We first solve the dimensionless model and estimate its parameters for an uncycled cell using impedance data at multiple states of charge. For this case, all estimate parameters correspond to the reference cell with no degradation. We then proceed to estimate model parameters for the aged cells.

The model fits the data well for all the states of charge (Figs. 3a–3c). The parameters (Z^* , $\Theta_{11,p}$, $\Theta_{11,n}$, Θ_{14}) that are estimated from this dataset are consistent for all the curves, as the EIS responses are relatively similar for all SOCs. As explained earlier, these parameters are not likely to change as the cell ages. Any change in them from estimation algorithm are likely due to the model not being sensitive to these parameters within the range of frequencies in the data. When EIS spectrum is relatively non-sensitive to a parameter, the parameter is “free” to change within the routine as the estimation algorithm can still guess slightly different value without affecting fitting error much. To avoid any unrealistic variation, the values are averaged (Fig. 3d) from estimation from multiple SOCs (dataset A) and held constant throughout the estimation of parameters for battery degradation (dataset B). This approach precludes the need to know the individual cell design values, even under the reference conditions. The ability to include Z^* as part of the parameter set estimated, significantly expands the capability of this toolset to study aging in cells whose component level data is not available.

In dataset B, EIS response is obtained at 50% SOC at every 200 cycles. The algorithm is run until a convergence tolerance of 10^{-4} is reached on the *reduced chi-squared* value. The parameters estimated by the algorithm are sufficiently optimized to approximate the

experimental data quite well (Fig. 4). The error between data and model can be further improved by using better parameter estimation algorithms. Each parameter from these model fits is plotted with number of cycles in Figs. 5 and 6 to analyze the variation of battery internal states as the cell ages.

It can be observed that Θ_2 has almost no change in its value, which makes sense as the value of a small oscillating current does not change the linear response of a battery. Parameters like Θ_1 , Θ_4 , Θ_5 , Θ_6 also have very little change in value with number of cycles. Some of these parameters (like transference number, electrolyte diffusivity) can change physically but the model might not capture those changes due to EIS response within the measured frequency range not being sensitive to these parameters.

Θ_3 , corresponding to the ratio of solid phase conductivity to ionic conductivity, is a predominant factor controlling changes in the real part of impedance especially at high frequencies. The trend for Θ_3 is quite linear and its value increases about 60% in these 1000 cycles. The increase in Θ_3 with number of cycles showing that the effective ionic conductivity goes down with time as battery ages, leading to an increase in internal resistance.

The parameters Θ_7 , Θ_8 , Θ_9 and Θ_{10} , have a greater change within the cathode as compared to the anode which suggests that the cathode (NMC 811) degradation is more severe for this cell compared to anode (LTO). Θ_{10} relates to solid phase diffusion in electrode particles. We can observe decreasing trend in $\Theta_{10,p}$ suggesting a reduction of solid phase diffusivity. This could be a result of cathode degradation and fracture of particles due to rapid expansion and contraction during fast cycles. After first 200 cycles

(possibly after crack initiation), the degradation is severe, causing rapid reduction in $\Theta_{10,p}$.

Θ_7 and Θ_9 relating to charge transfer resistance drop gradually in the cathode as the battery ages, indicating that charge transfer resistance is increasing. It is suggested that the increase of cathode charge transfer resistance is caused by degradation in the cathode surface, such as rock-salt layer by positive electrode structure change or film-growth reaction by electrolyte.^{30,32,33} $\Theta_{8,p}$ (proportional to double layer capacitance) is seen to be decreasing within the cathode initially and slightly increase after 800 cycles. These changes (Θ_7 , Θ_8 , Θ_9 , and Θ_{10}) are not that significant (<40% change) within negative electrode (LTO) and can be attributed to the fact that LTO is known to be a zero-strain insertion material^{34,35} and known not to form SEI unless subject to potentials below 1 V.³⁶

Θ_{12} (electrode porosity) remains constant as the battery ages, but reduces near 1000 cycles, and again the drop is more prominent in positive electrode suggesting a reduction in cathode porosity. But it is possible that this change is not physical and is a result of parameter estimation algorithm not finding a sufficiently optimized solution for the 1000 cycle case (see Figs. 4a and 4c), which could also be affecting Θ_8 . Bruggeman constant (Θ_{15}) is not seen to change much.

The model provides understanding of physical changes in the cell and can hence serve as a useful diagnostic tool to understand dominant degradation mode, by eliminating/reducing the number of complex experiments involving cell teardowns. Along with this, the approach can be potentially used to make real-time predictions during EV operation. To achieve this, we can use fitting functions on of parameter trends which can then be extrapolated into the future. For demonstrative purposes a simple analysis is shown in Fig. 7, using the same dataset B, where we attempt to use data from up to 600 cycles and make a prediction of parameters for 800 cycles and 1000 cycles. The following fitting function is used for all parameters.

$$\log(\theta_i) = m N_{\text{cycle}} + b \quad [17]$$

In theory, depending on degradation mechanisms, we will need to use more suitable functions for each parameter. In this case, prediction of EIS spectrum at 800 cycles has small error compared to data, which is further exacerbated at 1000 cycles. But it should be noted that this dataset is limited to just a few EIS curves and all parameters' trends are captured using a very simple function. Applying this approach to larger data sets will allow us to identify appropriate fitting functions that capture trends in these parameters well. These models can then be used to predict how parameters evolve with time and estimate how battery is expected to age in the future based on past changes in EIS spectrum.

Figure 8 provides a high-level overview of the approach used in this paper. A non-dimensionalized model developed in this study predicts cell impedance as a function of frequency based on 22 input parameters. Coupled with a Levenberg-Marquart parameter estimation routine, these parameters can be guessed such that the model finds a good fit to a given EIS curve. It is important to identify which of these parameters do not change with aging, so that these can be held constant to analyze aging dataset. We identify 4 such parameters and predict their averaged values using a separate dataset. These values are held constant while the rest are estimated to provide the best fit for aging dataset (EIS curves at multiple cycle numbers). Finally, the changes in estimated parameters are analyzed to provide insights for understanding dominant degradation mechanisms.

Conclusions

An approach to understanding battery physics from EIS data using physics-based modeling has been developed. The model is generic and can be extended to various battery chemistries and with varying properties along the thickness direction. This approach allows us to gain valuable insights and use physics-based models

without having prior knowledge of the battery chemistry, format, or capacity. This model can be used to understand battery aging in terms of changes in physics-based parameters. We can extend the model by modifying the form of particle impedance. This framework still has limitations such as being sensitive to initial guess values for parameter estimation because of the algorithm finding local minima, as well as multiple parameters sets predicting similar EIS response. The model needs to be applied to a wide range of data to improve the accuracy of estimated parameters. Further, when applied to a large number of data points, it can be used as a predictive tool during battery operation to understand state of health and battery life.

Appendix. Dimensional Equations for Pseudo two-Dimensional Impedance Model²⁶

Governing Equations

$$\frac{\partial}{\partial x} \left(\sigma^{\text{eff}} \frac{\partial \tilde{\phi}_1}{\partial x} \right) = a F \tilde{c}_1$$

$$-\frac{\partial}{\partial x} \left(\sigma^{\text{eff}} \frac{\partial \tilde{\phi}_1}{\partial x} \right) - \frac{\partial}{\partial x} \left(\kappa_e^{\text{eff}} \frac{\partial \tilde{\phi}_1}{\partial x} \right) + \frac{\partial}{\partial x} \left(\frac{2\kappa_e^{\text{eff}} RT(1-t_+) \tilde{c}_2}{F c_0} \frac{\partial \tilde{c}_2}{\partial x} \right) = 0$$

$$i\omega \tilde{c}_2 = \frac{\partial}{\partial x} \left(D_e^{\text{eff}} \frac{\partial \tilde{c}_2}{\partial x} \right) + a \tilde{j} (1-t_+) \left[\frac{\partial \tilde{c}_2}{\partial x} \right]_{x=0^+} = 0$$

$$i\omega \tilde{c}_1 = \frac{D_s}{r^2} \frac{\partial}{\partial r} \left(r^2 \frac{\partial \tilde{c}_1}{\partial r} \right)$$

Boundary Conditions

$$\left[\frac{\partial \tilde{\phi}_1}{\partial x} \right]_{x=0^+} = -\frac{I_{\text{app}}}{\sigma_n^{\text{eff}}}$$

$$\left[\frac{\partial \tilde{\phi}_1}{\partial x} \right]_{x=l_n^-} = 0$$

$$\left[\frac{\partial \tilde{\phi}_1}{\partial x} \right]_{x=(l_n+l_s)^+} = 0$$

$$\left[\frac{\partial \tilde{\phi}_1}{\partial x} \right]_{x=(l_n+l_s+l_p)^-} = -\frac{I_{\text{app}}}{\sigma_p^{\text{eff}}}$$

$$\tilde{\phi}_2 = 0$$

$$\kappa_{e,n}^{\text{eff}} \left[\frac{\partial \tilde{\phi}_2}{\partial x} \right]_{x=l_n^-} = \kappa_{e,s}^{\text{eff}} \left[\frac{\partial \tilde{\phi}_2}{\partial x} \right]_{x=l_n^+}$$

$$\kappa_{e,s}^{\text{eff}} \left[\frac{\partial \tilde{\phi}_2}{\partial x} \right]_{x=(l_n+l_s)^-} = \kappa_{e,p}^{\text{eff}} \left[\frac{\partial \tilde{\phi}_2}{\partial x} \right]_{x=(l_n+l_s)^+}$$

$$\left[\frac{\partial \tilde{\phi}_2}{\partial x} \right]_{x=(l_n+l_s+l_p)^-} = 0$$

$$D_{e,n}^{\text{eff}} \left[\frac{\partial \tilde{c}_2}{\partial x} \right]_{x=l_n^-} = D_{e,s}^{\text{eff}} \left[\frac{\partial \tilde{c}_2}{\partial x} \right]_{x=l_n^+}$$

$$D_{e,s}^{\text{eff}} \left[\frac{\partial \tilde{c}_2}{\partial x} \right]_{x=(l_n+l_s)^-} = D_{e,p}^{\text{eff}} \left[\frac{\partial \tilde{c}_2}{\partial x} \right]_{x=(l_n+l_s)^+}$$

$$\left[\frac{\partial \tilde{c}_2}{\partial x} \right]_{x=(l_n+l_s+l_p)^-} = 0$$

$$\left[\frac{\partial \tilde{c}_1}{\partial r} \right]_{r=0} = 0$$

$$\left[\frac{\partial \tilde{c}_1}{\partial r} \right]_{r=R_s} = \tilde{j}$$

ORCID

Anudeep Mallarapu  <https://orcid.org/0000-0003-3861-4748>

Yohei Uemura  <https://orcid.org/0000-0002-4101-8237>

References

1. M. Gaberšček, "Understanding Li-based battery materials via electrochemical impedance spectroscopy." *Nat. Commun.*, **12**, 6513 (2021).
2. N. Meddings et al., "Application of electrochemical impedance spectroscopy to commercial Li-ion cells: A review." *J. Power Sources*, **480**, 228742 (2020).
3. A. M. Colclasure, A. R. Dunlop, S. E. Trask, B. J. Polzin, A. N. Jansen, and K. Smith, "Requirements for enabling extreme fast charging of high energy density li-ion cells while avoiding lithium plating." *J. Electrochem. Soc.*, **166**, A1412 (2019).
4. A. Mallarapu, V. S. Bharadwaj, and S. Santhanagopalan, "Understanding extreme fast charge limitations in carbonate mixtures." *J. Mater. Chem. A*, **9**, 4858 (2021).
5. J. S. Edge et al., "Lithium ion battery degradation: what you need to know." *Phys. Chem. Chem. Phys.*, **23**, 8200 (2021).
6. J. M. Allen et al., "Quantifying the influence of charge rate and cathode-particle architectures on degradation of Li-ion cells through 3D continuum-level damage models." *J. Power Sources*, **512**, 230415 (2021).
7. L. Mu et al., "Oxygen release induced chemomechanical breakdown of layered cathode materials." *Nano Lett.*, **18**, 3241 (2018).
8. D. P. Finegan et al., "Spatial dynamics of lithiation and lithium plating during high-rate operation of graphite electrodes." *Energy Environ. Sci.*, **13**, 2570 (2020).

9. R. Xiong, J. Tian, H. Mu, and C. Wang, "A systematic model-based degradation behavior recognition and health monitoring method for lithium-ion batteries." *Appl. Energy*, **207**, 372 (2017).
10. H. Sun et al., "Quantitative analysis of degradation modes of lithium-ion battery under different operating conditions." *Energies*, **14**, 1 (2021).
11. U. Tröltzsch, O. Kanoun, and H. R. Tränkle, "Characterizing aging effects of lithium ion batteries by impedance spectroscopy." *Electrochim. Acta*, **51**, 1664 (2006).
12. E. Teliz, C. F. Zinola, and V. Díaz, "Identification and quantification of ageing mechanisms in Li-ion batteries by Electrochemical impedance spectroscopy." *Electrochim. Acta*, **426**, 140801 (2022).
13. S. Santhanagopalan, Q. Guo, P. Ramadass, and R. E. White, "Review of models for predicting the cycling performance of lithium ion batteries." *J. Power Sources*, **156**, 620 (2006).
14. M. Doyle, T. F. Fuller, and J. Newman, "Modeling of galvanostatic charge and discharge of the lithium/polymer/insertion cell." *J. Electrochem. Soc.*, **140**, 1526 (1993).
15. W. Mai, A. Colclasure, and K. Smith, "A reformulation of the pseudo2D battery model coupling large electrochemical-mechanical deformations at particle and electrode levels." *J. Electrochem. Soc.*, **166**, A1330 (2019).
16. V. R. Subramanian, V. Boovaragavan, V. Ramadesigan, and M. Arabandi, "Mathematical model reformulation for lithium-ion battery simulations: galvanostatic boundary conditions." *J. Electrochem. Soc.*, **156**, A260 (2009).
17. J. Kim, A. Mallarapu, S. Santhanagopalan, and J. Newman, "A robust numerical treatment of solid-phase diffusion in pseudo two-dimensional lithium-ion battery models." *J. Power Sources*, **556**, 232413 (2023).
18. A. Mallarapu, J. Kim, K. Carney, P. DuBois, and S. Santhanagopalan, "Modeling extreme deformations in lithium ion batteries." *eTransportation*, **4**, 100065 (2020).
19. J. Kim, A. Mallarapu, and S. Santhanagopalan, "Transport processes in a li-ion cell during an internal short-circuit." *J. Electrochem. Soc.*, **167**, 090554 (2020).
20. G. H. Kim, K. Smith, K. J. Lee, S. Santhanagopalan, and A. Pesaran, "Multi-domain modeling of lithium-ion batteries encompassing multi-physics in varied length scales." *J. Electrochem. Soc.*, **158**, A955 (2011).
21. P. J. Weddle, R. J. Kee, and T. Vincent, "A stitching algorithm to identify wide-bandwidth electrochemical impedance spectra for li-ion batteries using binary perturbations." *J. Electrochem. Soc.*, **165**, A1679 (2018).
22. M. Doyle, J. P. Meyers, and J. Newman, "Computer simulations of the impedance response of lithium rechargeable batteries." *J. Electrochem. Soc.*, **147**, 99 (2000).
23. J. P. Meyers, M. Doyle, R. M. Darling, and J. Newman, "The impedance response of a porous electrode composed of intercalation particles." *J. Electrochem. Soc.*, **147**, 2930 (2000).
24. J. Huang et al., "Editors' choice—review—impedance response of porous electrodes: theoretical framework, physical models and applications." *J. Electrochem. Soc.*, **167**, 166503 (2020).
25. L. Teo, V. R. Subramanian, and D. T. Schwartz, "Dynamic electrochemical impedance spectroscopy of lithium-ion batteries: revealing underlying physics through efficient joint time-frequency modeling." *J. Electrochem. Soc.*, **168**, 010526 (2021).
26. M. Pathak et al., "Fast impedance simulation of lithium-ion batteries with pseudo-two dimensional electrochemical models." *J. Electrochem. Soc.*, **165**, A1324 (2018).
27. E. Ayerbe, F. Varas, and I. Urdampilleta, "On the use of dimensionless parameters for fast battery performance analysis." *J. Electrochem. Soc.*, **168**, 100515 (2021).
28. M. Doyle and J. Newman, "Analysis of capacity-rate data for lithium batteries using simplified models of the discharge process." *J. Appl. Electrochem.*, **27**, 846 (1997).
29. G. Sikha and R. E. White, "Analytical expression for the impedance response for a lithium-ion cell." *J. Electrochem. Soc.*, **155**, A893 (2008).
30. S. Morimoto, Y. Kanai, M. Yoshiki, M. Oki, and R. Yagi, "(Digital presentation) accelerated degradation mechanism of Ni-Rich Ncm cathode materials at high and low voltage range combined cycling for li-ion batteries." *ECS Meet. Abstr.*, **MA2022-01**, 382 (2022).
31. R. Shrager, A. Jutan, R. Muzic, and O. Till, "leasqr.m" (1992-2016), OctaveForge, A collection of packages providing extra functionality for GNU Octave.
32. F. Friedrich et al., "Editors' choice—capacity fading mechanisms of NCM-811 cathodes in lithium-ion batteries studied by X-ray diffraction and other diagnostics." *J. Electrochem. Soc.*, **166**, A3760 (2019).
33. H. Kuriyama et al., "Observation of anisotropic microstructural changes during cycling in $\text{LiNi}_{0.5}\text{Co}_{0.2}\text{Mn}_{0.3}\text{O}_2$ cathode material." *J. Power Sources*, **275**, 99 (2015).
34. T. Ohzuku, A. Ueda, and N. Yamamoto, "Zero-strain insertion material of $\text{Li}[\text{Li}_{1/3}\text{Ti}_{5/3}]\text{O}_4$ for rechargeable lithium cells." *J. Electrochem. Soc.*, **142**, 1431 (1995).
35. A. Ghosh and F. Ghamouss, "Role of electrolytes in the stability and safety of lithium titanate-based batteries." *Front. Mater.*, **7**, 1 (2020).
36. S. Wang, K. Yang, F. Gao, D. Wang, and C. Shen, "Direct visualization of solid electrolyte interphase on $\text{Li}_4\text{Ti}_5\text{O}_{12}$ by: In situ AFM." *RSC Adv.*, **6**, 77105 (2016).